

## The mixed layer salinity budget and sea ice in the Southern Ocean

Li Ren,<sup>1,2</sup> Kevin Speer,<sup>1</sup> and Eric P. Chassignet<sup>1,3</sup>

Received 2 September 2010; revised 19 May 2011; accepted 2 June 2011; published 26 August 2011.

[1] The seasonal variation of the mixed layer salinity budget in the Southern Ocean is evaluated over the latitude range 45°S–62°S using Argo profiling float data, freshwater fluxes (evaporation minus precipitation (E-P)), geostrophic velocity, wind stress, and sea ice concentration observations. The seasonal cycle of the mixed layer salinity is driven by seasonality in E-P, Ekman advection, entrainment, and sea ice. Over large areas, the geostrophic advection and diffusion show smaller contributions to the seasonal variation relative to other terms. The air-sea freshwater flux and Ekman advection in this area generally result in net decreases in salinity, while the entrainment term yields increases. Residual imbalance is consistent with a sea ice effect, whose contribution is evaluated. Sea ice is found to make a significant contribution, growing in importance toward the ice edge.

**Citation:** Ren, L., K. Speer, and E. P. Chassignet (2011), The mixed layer salinity budget and sea ice in the Southern Ocean, *J. Geophys. Res.*, 116, C08031, doi:10.1029/2010JC006634.

### 1. Introduction

[2] Upper ocean salinity has gained increasing attention in recent years as the relationships between the world's oceans and climate change are explored. In the Southern Ocean, salinity plays an important role in the stabilization of the upper ocean column, particularly in the Antarctic Zone south of the Polar Front. Furthermore, changes in salinity may indicate changes in the hydrologic cycle, a key agent in climate change. Salinity variations are driven by a variety of sources at the surface, including air-sea fluxes, sea ice formation and melting, and melting glacial ice. Antarctic sea ice has a very strong seasonal cycle and salinity variations in the seasonal sea ice zone and beyond might be expected to show some relation to this forcing. Sea ice around the Antarctic continent plays a key role in driving global ocean circulation through its control on bottom water formation. It also buffers heat and momentum exchange across the ocean surface and can drift, producing additional sources of freshwater to regions distant from the area of formation.

[3] In the ocean surrounding the Antarctic continent, sea ice has shown significant regional changes in recent times, as observed by satellites post-1978, but the net change is small [Comiso and Nishio, 2008]. Relatively strong melt in the Pacific sector west of the Antarctic Peninsula has occurred, whereas sea ice extent has grown farther west in the Ross Sea region [Stammerjohn *et al.*, 2008]. Decreasing salinity in the Southern Ocean is thought to be due to increasing precipitation [Banks and Bindoff, 2003; Böning *et al.*, 2008] and also

to regional melting of glacial ice [Jacobs and Giulivi, 2010]. The true contributions of ice melt and air-sea evaporation and precipitation fluxes to changing ocean salinity are not well known. In the future, strong decreases in sea ice cover could occur as greenhouse gas-driven atmospheric forcing dominates the response of the Southern Ocean [Turner *et al.*, 2009].

[4] In the Southern Ocean, upper ocean salinity variations have been more difficult to quantify than elsewhere due to the more limited number of observations. Durack and Wijffels [2010] recently documented the global trends in salinity, drawing upon the modern extensive Argo data set and providing a global context for earlier observations [e.g., Wong *et al.*, 1999] of decreasing salinity in waters spreading away from the Southern Ocean. Seasonality of the air-sea flux is strong at high latitudes and potentially fundamental to the salinity balance, although a greater understanding of the various sources during the year is needed. The seasonal variation in Southern Ocean sea ice cover is among the largest seasonal cycles on Earth's surface, and small shifts in the seasonal cycle, related for instance to ocean, wind or atmospheric radiation variability, could have a significant impact on upper ocean salinity.

[5] Advective and diffusive processes operate in the surface mixed layer to redistribute freshwater or salinity. In rough terms, strong geostrophic transport dominates the zonal advection and tends to make all properties uniform in longitude, while Ekman transport controls net meridional advection. Rintoul and England [2002] showed that Ekman advection in the region south of Australia plays a dominant role in both the heat and salt budget. Sallée *et al.* [2006] documented the processes controlling the mixed layer heat budget in the Indian Ocean region and quantified the effects of air-sea fluxes, advection and eddy diffusive terms. Dong *et al.* [2009] discussed the seasonal mixed layer salt budget in the Southern Ocean integrated over large areas and emphasized the Ekman control and local air-sea fluxes. However, since they did not directly quantify the role of the sea ice, Dong *et al.* [2009] were unable to describe the

<sup>1</sup>Department of Earth, Ocean and Atmospheric Science, Florida State University, Tallahassee, Florida, USA.

<sup>2</sup>Now at Earth System Science Interdisciplinary Center, Cooperative Institute for Climate and Satellites, University of Maryland, College Park, Maryland, USA.

<sup>3</sup>Center for Ocean-Atmospheric Prediction Studies, Florida State University, Tallahassee, Florida, USA.

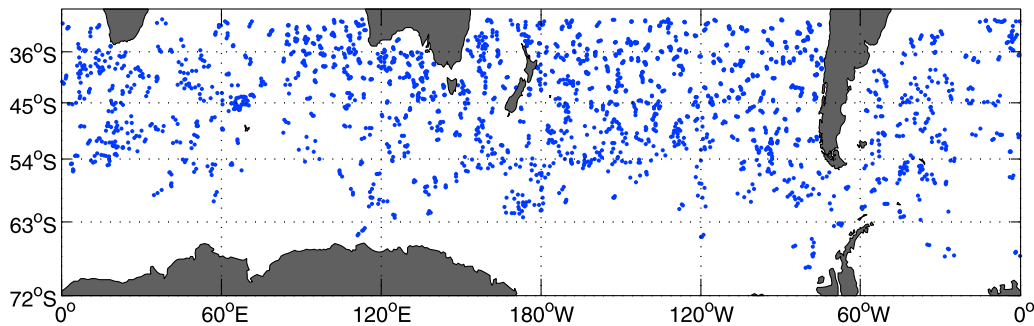


**Figure 1.** Selected Argo float profile's spatial distribution in November 2008.

contribution of this source to the upper ocean salinity balance. In this paper, we revisit the upper ocean salinity balance with the goal of examining these transport processes in greater detail, discriminating regional differences, and considering the role of the seasonal sea ice melting and freezing cycle in the balance. In addition, a longer time period of Argo profiling float data and more net freshwater flux products are employed in this study to improve the mixed layer salinity budget and error estimates.

[6] To represent sea ice in the mixed layer salinity budget, we take a straightforward vertically integrated view. The equation for salinity may be written as

$$\frac{\partial S_m}{\partial t} = \frac{(E - P)S_m}{h_m} - u_e \cdot \nabla S_m - u_g \cdot \nabla S_m - \frac{w_e \Delta S}{h_m} + \kappa \nabla^2 S_m + \frac{I S_m}{h_m}, \quad (1)$$

where  $E$  is evaporation,  $P$  is precipitation,  $S_m$  is salinity in the mixed layer (mean salinity within the mixed layer),  $u_e$  is the Ekman velocity,  $u_g$  is the geostrophic velocity,  $w_e$  is the entrainment velocity, and  $\Delta S$  is the salinity difference between the average salinity within the mixed layer and 15 m below the base of the mixed layer. The choice of a salinity reference of 15 m below the base of the mixed layer is discussed in Appendix A.  $I$  is the sea ice contribution in units of  $\text{ms}^{-1}$ . Positive  $I$  means that sea ice is freezing and removing freshwater from the ocean; negative  $I$  means that sea ice is melting and adding freshwater to the ocean. A detailed explanation of the sea ice term will be provided in section 2. The term on the left-hand side of equation (1) represents the salinity tendency; the terms on the right-hand side represent net air-sea freshwater flux ( $E-P$ ), Ekman advection, geostrophic advection, entrainment, horizontal diffusion, and sea ice formation and melt.

[7] The main goal of this paper is to study the seasonal variation of the mixed layer salinity budget during 2006–2010 in the Southern Ocean, and the role of sea ice. It is organized as follows: section 2 presents the seasonal variation of the near-sea surface salinity; section 3 describes the seasonal variation of the mixed layer salinity budget; and section 4 contains a summary and discussion.

## 2. Seasonal Variation of Near-Sea Surface Salinity

### 2.1. Data

[8] The seasonal variation of near-surface salinity in the Southern Ocean is analyzed using the 5 years (2006–2010) of

Argo float data. Argo is a global array of freely drifting floats that measure the temperature and salinity of the upper 2000 m of the ocean [Gould *et al.*, 2004]. Since 2006, the Argo float measurements in the Southern Ocean are more numerous and more evenly distributed, providing important full seasonal coverage with winter measurements, and a high quality data set for a large spatial scale study of the upper ocean heat and salt balances in this region where historical ship-based observations were biased to summer. Spatial coverage, however, is still mainly limited to the region outside the sea ice zone itself. We do not consider here the growing data set resulting from the animal-borne sensor programs [Charrassin *et al.*, 2008].

[9] Five years of Argo float profiles from January 2006 to December 2010 are used. The observations are distributed fairly evenly up to about 62°S hence we restrict the analysis to the latitude band of 30°S to 62°S. We eliminate the measurements under the sea ice. All the selected profiles are binned monthly. The number of profiles in each month gradually increases with time, with a mean of 2228 in November 2008, a minimum of 1554 in February 2006, and a maximum of 2821 in March 2010. Figure 1 shows the locations of the profiles in November 2008, midway through this time period. We expect that large-scale spatial features north of 62°S are captured by this data set.

[10] The Argo floats profile near the surface, but do not measure sea surface salinity. The percentages of profiles that measure the T/S shallower than depths of 5 m, 10 m, and 15 m are 56.7%, 98.7% and 99.4% of the total profiles, respectively. In order to use as many as profiles as possible, the 15 m depth salinity ( $S_{15}$ ) is selected for the purpose of describing the seasonal variation of the surface salinity.

[11] The monthly, binned  $S_{15}$  are objectively mapped onto a 1° by 1° grid in the area south of 30°S to 62°S. The objective mapping uses a Poisson function with a length scale of 6° in longitude and 3° in latitude [Bretherton *et al.*, 1976]. A second order polynomial is assumed for the large-scale background field [Le Traon, 1990].

### 2.2. Seasonal Variation

[12] Figures 2a and 2b show the  $S_{15}$  in summer and winter, respectively. The summer is defined as January, February and March; winter is defined as July, August and September throughout this paper. In both summer and winter, the near-surface salinity is higher in the subtropical area and lower at higher latitudes along the Antarctic Circumpolar Current (ACC). At higher latitudes the ocean is fresher in summer

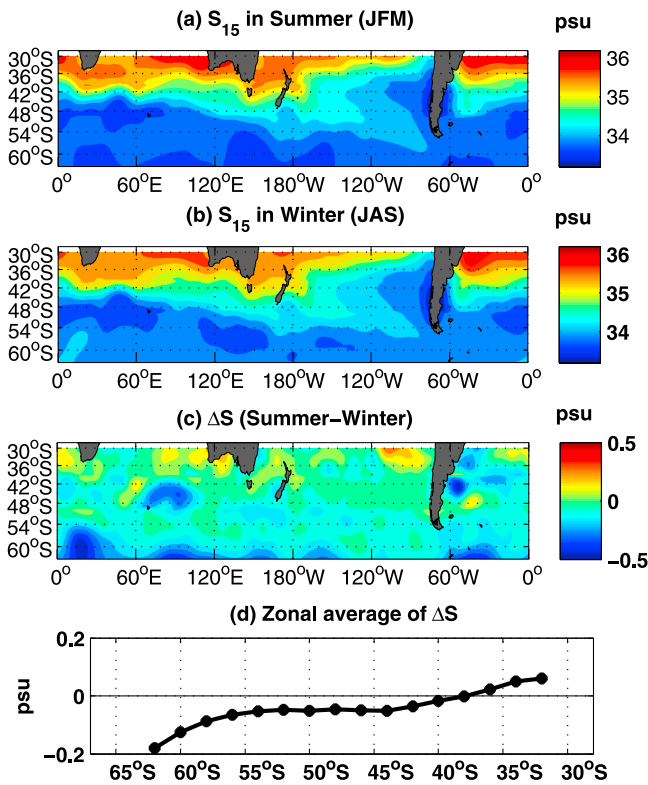


**Figure 2.** Monthly mean and seasonal variations of  $S_{15}$  estimated from Argo float data: (a)  $S_{15}$  in summer, averaged for January, February, and March from 2006 to 2010; (b)  $S_{15}$  in winter, averaged for July, August, and September from 2006 to 2010; (c) the difference between summer and winter, estimated by subtracting the salinity in winter from summer; and (d) zonal average of the salinity difference between summer and winter (Figure 2c) at the latitude interval  $2^\circ$ .

compared to winter (Figure 2c), while salinity in the subtropical band shows little seasonal variation.

[13] The amplitude of the seasonal variation is shown as the difference between summer and winter (Figure 2c). The summer freshening is an outstanding feature in the Southern Ocean, becoming stronger toward the south and zonally distributed. Thus, the zonal average seasonal variation (Figure 2d) indicates that the salinity decrease in summer is strongest near  $62^\circ\text{S}$  and weaker toward the equator. The zonal average seasonal variation is relatively larger (greater than

0.05 psu) south of  $45^\circ\text{S}$  and approaches zero around  $38^\circ\text{S}$ . The domain- ( $45^\circ\text{S}$ – $62^\circ\text{S}$ ) averaged  $S_{15}$  (Figure 3) shows an annual period variation, with a mean and standard deviation of 34.03 psu and 0.03 psu.  $S_{15}$  is lower in summer (JFM) and higher in winter (JAS). The annual variation accounts for 90% of the total variance (Figure 3).

[14] Such seasonal variation can be caused by several factors. However, the character of the seasonal variation indicates that the sea ice might play some role in controlling the near-surface salinity since the seasonal variation becomes stronger toward the sea ice zone.

### 3. Seasonal Variation of Mixed Layer Salinity Budget

[15] As the seasonal variation is the dominant variation of the near-surface salinity in the Southern Ocean, understanding the causes of such variation is important when investigating interannual, decadal and even longer time period variations. The seasonal variation seems very likely to be related to the sea ice formation and melt, at least closer to the continent. In this section, the mixed layer salinity budget is investigated using equation (1), with each term calculated from observations.

#### 3.1. Mixed Layer Depth, $\Delta S$ , and $S_m$

[16] Mixed layer depth ( $h_m$ ),  $\Delta S$ , and  $S_m$  in equation (1) are all calculated from the Argo profiling floats data. Mixed layer depth ( $h_m$ ) is defined from individual float profiles and determined as the depth with the density difference  $\Delta\rho = 0.03 \text{ kg m}^{-3}$  from the topmost near-surface value, consistent with other studies [de Boyer Montégut et al., 2004; Dong et al., 2008]. Other reasonable choices have been explored but have little impact on the results. The mixed layer depth in summer is generally shallower than 150 m depth (Figure 4a). In winter, the mixed layer depth is larger. The deeper mixed layers are mainly located within or north of the Antarctic Circumpolar Circulation (ACC) (Figure 4b). The maximum mixed layer depth in the Indian and Pacific sector is deeper than 400 m, while in the Atlantic sector the maximum mixed layer depth is little more than 150 m.

[17]  $S_m$  is calculated as the average salinity within the mixed layer in each profile. It has a similar spatial and temporal character as the near-surface salinity ( $S_{15}$ ). The distribution of  $S_{15}$  is presented in section 2.2. Salinity below the mixed layer base is needed for the entrainment term and is difficult to specify. Here, we specified the salinity at a depth

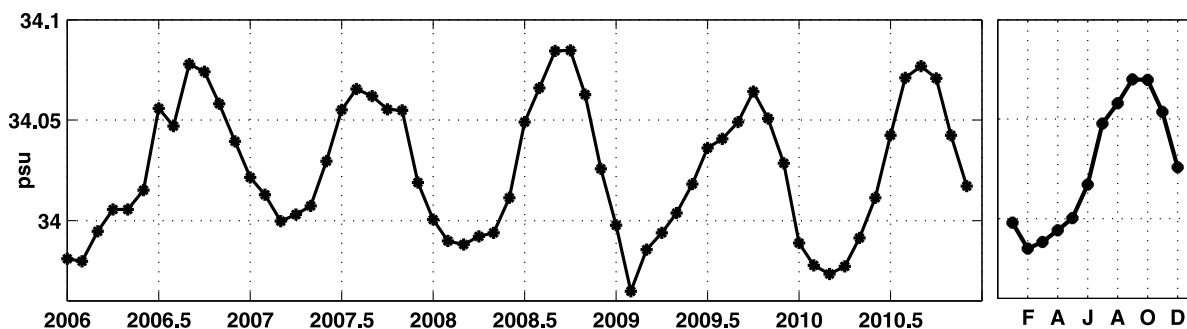


**Figure 3.** Domain ( $45^\circ\text{S}$ – $62^\circ\text{S}$ ) average of the  $S_{15}$ . (left) The monthly time series of  $S_{15}$  during 2006–2010 and (right) the corresponding estimated seasonal variation are shown.

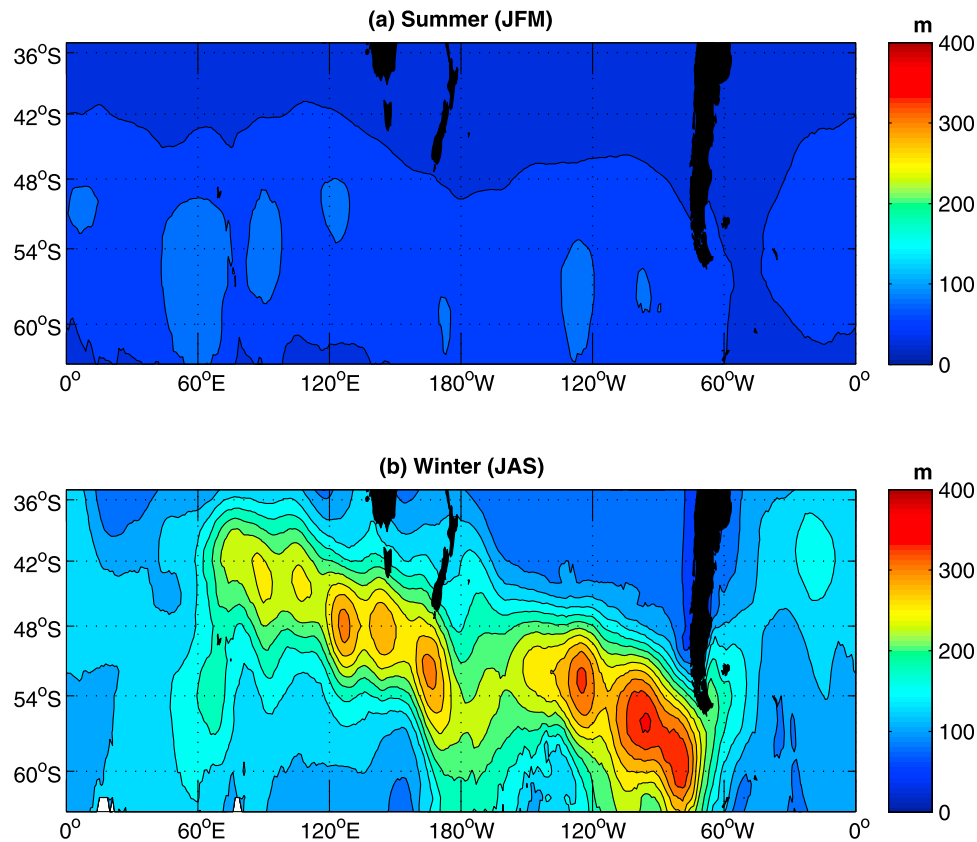


**Figure 4.** Mixed layer depth in (a) summer (JFM) and (b) winter (JAS). The summer mixed layer depth is the average of each January, February, and March and the winter mixed layer depth is the average of each July, August, and September during 2006–2010.

of 15 m below the mixed layer, based on an RMS imbalance in the mixed layer salinity budget (Appendix A and Figure 5). This choice gives an average salinity jump of 0.043 psu in June when the entrainment reaches its maximum.  $\Delta S$  is mostly positive north of 45°S in both summer and winter, where the salinity decreases with depth (Figure 5). This latitude band is characterized by a salinity minimum layer in the upper ocean. South of 45°S,  $\Delta S$  is mostly negative (except in parts of the southern Pacific Ocean in winter time), as the salinity increases with depth. The magnitudes of  $\Delta S$  become larger in winter (Figure 5b) as the mixed layer depth increases. In addition,  $\Delta S$  becomes significantly positive between 48°S and 55°S in the Pacific Ocean and north of 50°S in the Atlantic Ocean in winter (Figure 5b). This pattern is consistent with the significant deepening of the mixed layer depth in these two regions in winter (Figure 4).

[18] The  $S_m$ ,  $h_m$ , and  $\Delta S$  fields are objectively mapped onto a 1° by 1° grid in the area south of 30°S–62°S in the same way as  $S_{15}$  (section 2.1).

### 3.2. Freshwater Flux

[19] The net freshwater flux derives from evaporation (E) and precipitation (P). There are a number of freshwater flux products available, including monthly evaporation and precipitation from NCEP/NCAR reanalysis 1 [Kalnay et al., 1996], monthly evaporation and precipitation from NCEP-DOE reanalysis 2 [Kanamitsu et al., 2002], and synoptic monthly evaporation and precipitation from ECMWF Interim

reanalysis (ERA-Interim) [Berrisford et al., 2009]. Additionally, there are monthly precipitation data from the Climate Precipitation Center (CPC) Merged Analysis of Precipitation (CMAP) [Xie and Arkin, 1997, 1996] and Global Precipitation Climatology Project (GPCP) [Huffman et al. 1997; Adler et al., 2003], and monthly evaporation data from Objectively Analyzed air-sea Fluxes (OAFflux) [Yu and Weller, 2007]. Since the net freshwater flux is needed in the mixed layer salinity budget calculation, the monthly precipitation from GPCP and CMAP and the monthly evaporation from OAFflux are combined to make two sets of E-P. Thus, in total, there are five E-P sets used in this study, including NCEP1, NCEP2, ERA-Interim, OAFflux (E)-CMAP (P), and OAFflux (E)-GPCP (P). An objective choice is difficult to make without detailed comparisons with the appropriate meteorological observations, which are lacking. We choose the data set that minimizes the imbalance over a range of possible choices (see Appendix A for details) and assume that the air-sea flux data as a whole has larger errors in some sense than other terms. From the sensitivity test for the five sets of net freshwater flux, the OAFflux (E)–CMAP (P) results in the least RMS imbalance in the mixed layer salinity budget (Appendix A) and will be used in the salinity budget calculation.

### 3.3. Wind Stress

[20] We have used the QuikSCAT scatterometer pseudostress fields to estimate the Ekman velocity. The pseudostress

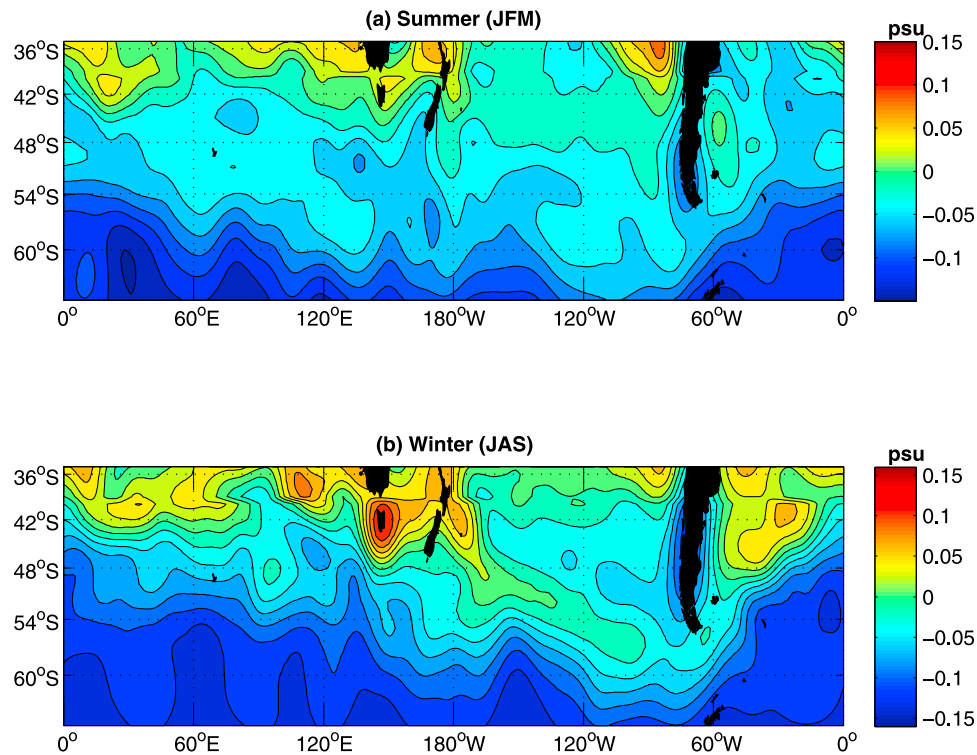


**Figure 5.**  $\Delta S$  in (a) summer (JFM) and (b) winter (JAS).  $\Delta S$  is defined as the salinity difference between average salinity within the mixed layer and 15 m below the base of the mixed layer.  $\Delta S$  in summer and winter are the average of each January, February, and March and July, August, and September during 2006–2010, respectively. The contour interval is 0.02 psu.

fields are objectively mapped onto a  $1^\circ \times 1^\circ$  grid [Pegion *et al.*, 2000] and can be obtained from the Florida State University Center for Ocean-Atmospheric Prediction Studies (COAPS). Monthly wind stress fields are computed from the pseudostress using parameters from Yelland and Taylor [1996].

[21] The Ekman velocity is calculated as

$$u_e = \frac{1}{\rho_0 f h_m} (\tau^y - \tau^x), \quad (2)$$

where  $\tau^x$  is the zonal wind stress,  $\tau^y$  is meridional wind stress,  $f$  is the Coriolis parameter, and  $\rho_0$  is the reference density of seawater, which is taken to be  $1027 \text{ kg m}^{-3}$ . Here  $h_m$  is mixed layer depth and, due to limited knowledge of Ekman depth in the Southern Ocean, is assumed to be equal to the Ekman depth. The salt budget is sensitive to the choice of the Ekman depth, especially when the Ekman depth is deeper than the mixed layer depth as the Ekman advection term will be overestimated [Dong *et al.*, 2009]. We expect that the opposite is predominantly true: the mixed layer depth is typically greater than the Ekman depth. The error associated with this choice is expected to be small.

[22] The meridional Ekman velocity dominates the zonal Ekman velocity in the ACC region, and becomes stronger in winter (Figure 6d). The spatial patterns of both zonal and meridional Ekman velocity do not change much between summer and winter (Figure 6), while the magnitudes become larger in winter.

### 3.4. Geostrophic Velocity

[23] The absolute geostrophic velocity from AVISO [Centre National d'Etudes Spatiales, 1996] has been used to estimate the monthly geostrophic advection. The absolute geostrophic velocity from AVISO employs different MDT (Mean Dynamical Topography) for our study period: for the time period January 2006 to May 2009, it uses the MDT based on Rio *et al.* [2005]; after May 2009, it uses the MDT based on Rio *et al.* [2009]. Fortunately, for the purpose of this study, the difference between the two MDTs does not impact the analysis, based on a sensitivity test including the data after May 2009. The data set is gridded at  $1/3^\circ$  by  $1/3^\circ$  resolution. Thus, in order to be consistent with other data sets used in this study, the AVISO geostrophic velocity was averaged on the same  $1^\circ$  grid as the Argo float data.

[24] The geostrophic velocity does not have much seasonal variation compared to the other variables used in the calculations: both the spatial pattern and magnitudes are roughly similar in winter and summer (Figure 7). The eastward zonal velocity dominates the meridional velocity along the ACC; magnitudes are typically  $10\text{--}20 \text{ cm s}^{-1}$  or more in the core of the ACC fronts.

### 3.5. Entrainment

[25] The entrainment velocity ( $w_e$ ) is calculated following Ren and Riser [2009]

$$w_e = H \left( \frac{\partial h_m}{\partial t} + \nabla \cdot h_m \vec{v} \right), \quad (3)$$

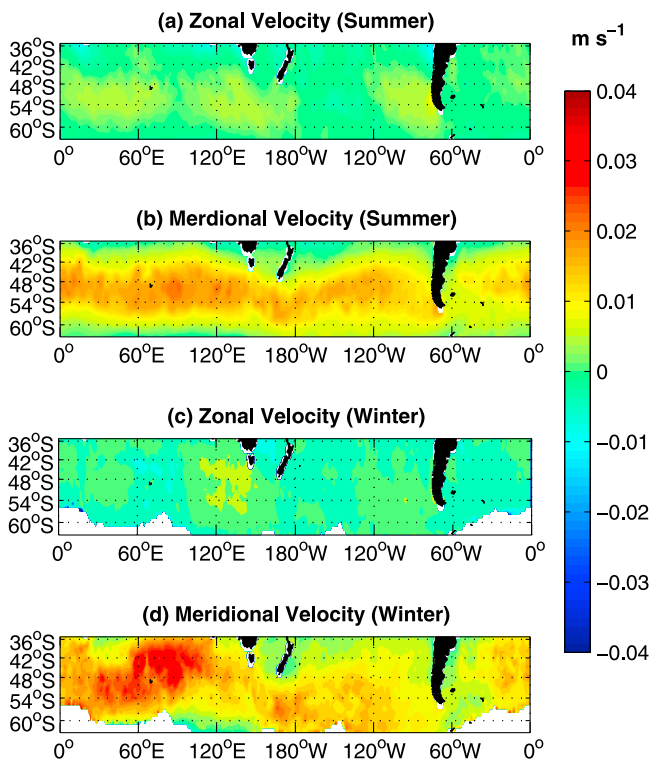


**Figure 6.** Ekman velocity in summer (JFM) for (a) zonal velocity and (b) meridional velocity and in winter (JAS) for (c) zonal velocity and (d) meridional velocity. Zonal and meridional velocities in summer are the average of each January, February, and March and zonal and meridional velocities in winter are the average of each July, August, and September during January 2006 to November 2009.

where  $\vec{v}$  is the horizontal velocity including Ekman velocity and geostrophic velocity.  $H$  is the Heaviside unit function and is defined as

$$H(x) = \begin{cases} 1, & x \geq 0 \\ 0, & x < 0. \end{cases} \quad (4)$$

Only positive velocities are considered and the detrainment (negative) velocity is set to zero, since the water that flows out from the base of the mixed layer has the same properties as the water in the mixed layer, and will not affect the mixed layer salinity. The annual mean entrainment velocity (Figure 8) shows values greater than  $10^{-5} \text{ m s}^{-1}$  upward velocity in the Pacific and Indian Ocean, less in the Atlantic Ocean, with a similar pattern as the deep winter mixed layer depth (Figure 4b). This suggests that  $\partial h_m / \partial t$  dominates  $\nabla \cdot h_m \vec{v}$  in the annual mean entrainment velocity, which was confirmed from the individual terms.

### 3.6. Sea Ice

[26] Sea ice is frozen seawater. It loses most of its salinity in the freezing process and when it melts it brings freshwater to the surface of the ocean. The sea ice mass at time  $t$  and location  $(x, y)$  can be written as  $Mass = \rho_{ice} V = \rho_{ice} \cdot C h_{ice} \cdot Area$ . Here,  $V(t, x, y)$  stands for the sea ice volume,  $C(t, x, y)$  is sea ice concentration,  $Area$  stands for the area whose sea ice concentration is  $C(t, x, y)$ ,  $\rho_{ice}$  is the sea ice density, and

$h_{ice}(t, x, y)$  is the sea ice thickness. The net freshwater flux contribution from sea ice is calculated as the summation of the local sea ice mass change and the net sea ice advection.

[27] The local sea ice mass change in a month can be derived as  $\frac{(C(t, x, y) h_{ice}(t, x, y) - C(t-1, x, y) h_{ice}(t-1, x, y)) \cdot Area \cdot \rho_{ice}}{\Delta t}$ . Here,  $\Delta t$  is the time interval of 1 month. To convert the sea ice mass change to the freshwater flux,  $I$  is written as

$$I_{local} = \frac{(C(t, x, y) h_{ice}(t, x, y) - C(t-1, x, y) h_{ice}(t-1, x, y)) \cdot Area \cdot \rho_{ice}}{Area \cdot \rho_{ice} \cdot \Delta t} = \frac{(C(t, x, y) h_{ice}(t, x, y) - C(t-1, x, y) h_{ice}(t-1, x, y))}{\Delta t}. \quad (5)$$

Equation (5) expresses the local sea ice contribution to the salt budget. Thus, both sea ice concentration and thickness are needed.

[28] Sea ice concentration data from the Advanced Microwave Scanning Radiometer for EOS (AMSR-E) beginning May 2002 are used here, calculated from brightness temperature based on the ARTIST Sea Ice (ASI) algorithm [Sprenn *et al.*, 2008]. In summer, sea ice covers most of the western Weddell Sea and the near-continental margins of the Bellingshausen Basin and Amundsen Sea (Figure 9a). In winter, the sea ice coverage greater than 90% concentration expands to nearly 60°S in most of the Antarctic, nearly 55°S in the Atlantic sector, and to 65°S in the west Antarctic region (Figure 9b).

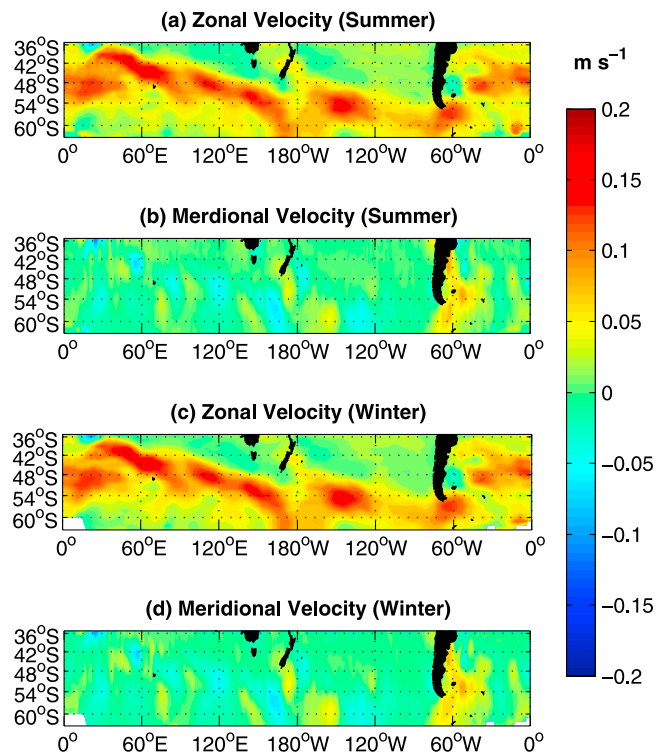


**Figure 7.** Geostrophic velocity in summer (JFM) for (a) zonal velocity and (b) meridional velocity and in winter (JAS) for (c) zonal velocity and (d) meridional velocity. Zonal and meridional velocities in summer are the average of each January, February, and March and zonal and meridional velocities in winter are the average of each July, August, and September during January 2006 to March 2010.

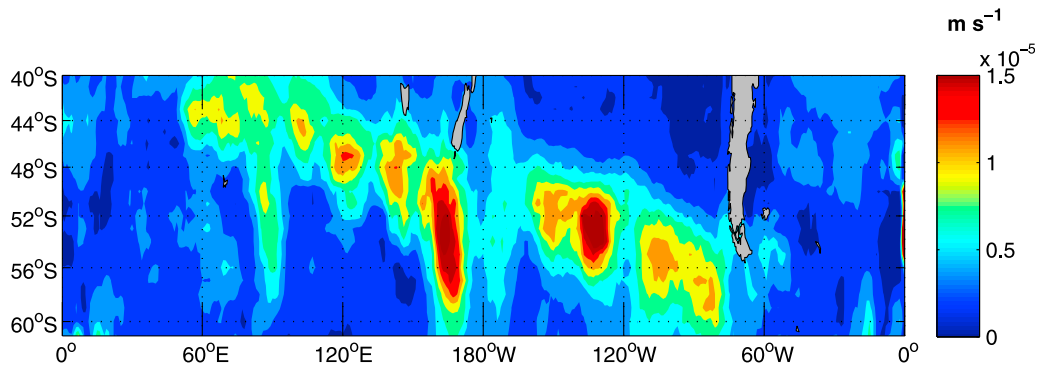


**Figure 8.** Annual mean entrainment velocity during January 2006 to November 2009.

[29] We make use of the sea ice thickness estimates from the Antarctic Sea Ice Processes & Climate (ASPeCt) program. This archived sea ice thickness data set contains 83 voyages and 2 helicopter flights from the period 1980–2005. *Worby et al.* [2008] documented the data quality control and processing. Data on thickness are very sparse and sampling is generally considered to be inadequate; however, some progress can be made by considering the climatological seasonal sea ice thickness cycle based on the existing observations. Tests with different choices of data statistics have been made to examine sensitivity. Due to the data limitations, only the annual variation of the sea ice thickness ( $h_{ice}$ ) is considered in this calculation. The annual mean spatial distribution of the sea ice thickness (Figure 10) shows the greatest sea ice thickness in the eastern Ross Sea and western Weddell Sea region. Sea ice thickness ranges from less than 1 m to about 2 m in other places along the Antarctic continent (Figure 10). The long-term mean sea ice thickness and standard deviation is  $0.87 \pm 0.91$  m [*Worby et al.*, 2008].

[30] The net sea ice advection is derived from  $\nabla \cdot (Mass U_{ice})$ , and the net freshwater flux from the sea ice advection is written as

$$I_{drift} = \frac{\nabla \cdot (\rho_{ice} C(t, x, y) h_{ice}(t, x, y) \cdot Area \cdot U_{ice}(t, x, y))}{\rho_{ice} Area} = \nabla \cdot (C(t, x, y) h_{ice}(t, x, y) \cdot U_{ice}(t, x, y)). \quad (6)$$

Sea ice drift ( $U_{ice}$ ) is assumed to be 3.0% of the wind speed with a turning angle  $23^\circ$  to the left of the wind direction [*Martinson and Wamser*, 1990]. The annual mean of (6) is shown in Figure 11. Sea ice divergence appears in the southeastern Weddell Sea and part of the western Ross Sea. The area within the minimum (summer) sea ice edge is shaded to avoid fast ice. Most of the area outside the summer sea ice edge is characterized by sea ice convergence, that is, a freshwater source (Figure 11). The greatest area of convergence is along the northern rim of the Weddell gyre, where the sea ice melt source is likely to be the result of sea ice drifting

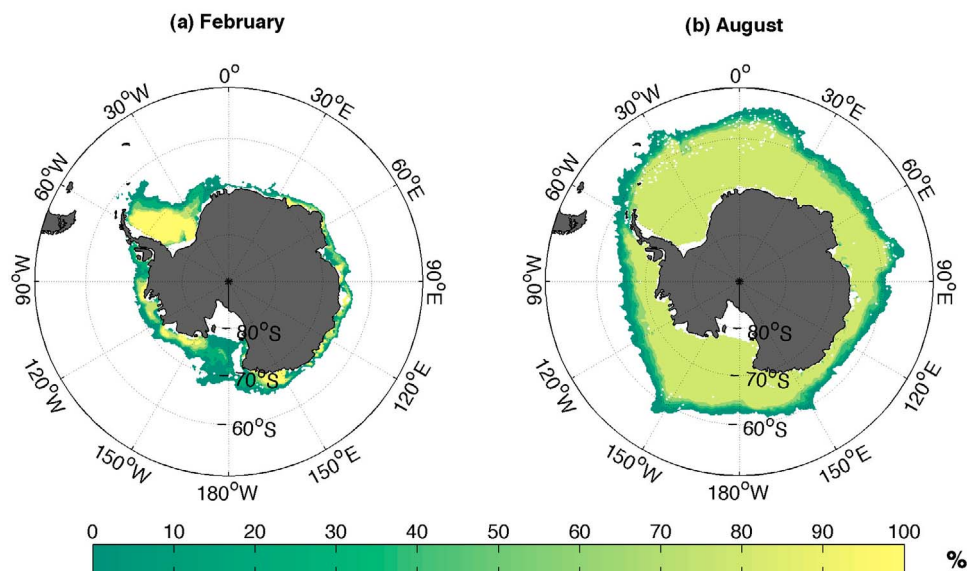


**Figure 9.** Sea ice concentration (%) in (a) February, which is estimated as the mean sea ice concentration of February from January 2006 to August 2010, and (b) August, which is estimated as the mean sea ice concentration of August from January 2006 to August 2010.

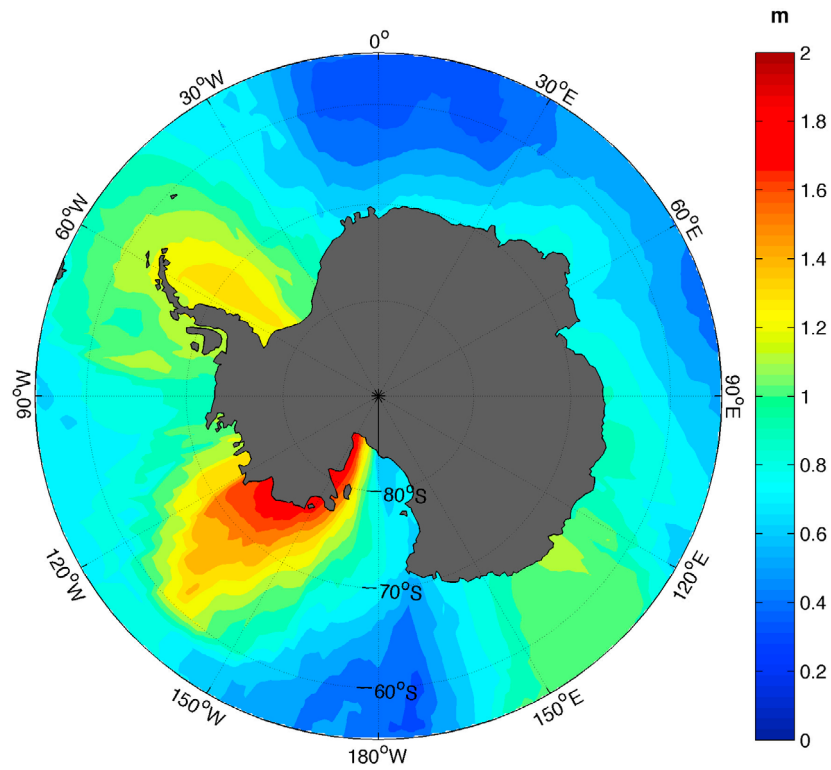


**Figure 10.** Annual mean sea ice thickness (m).

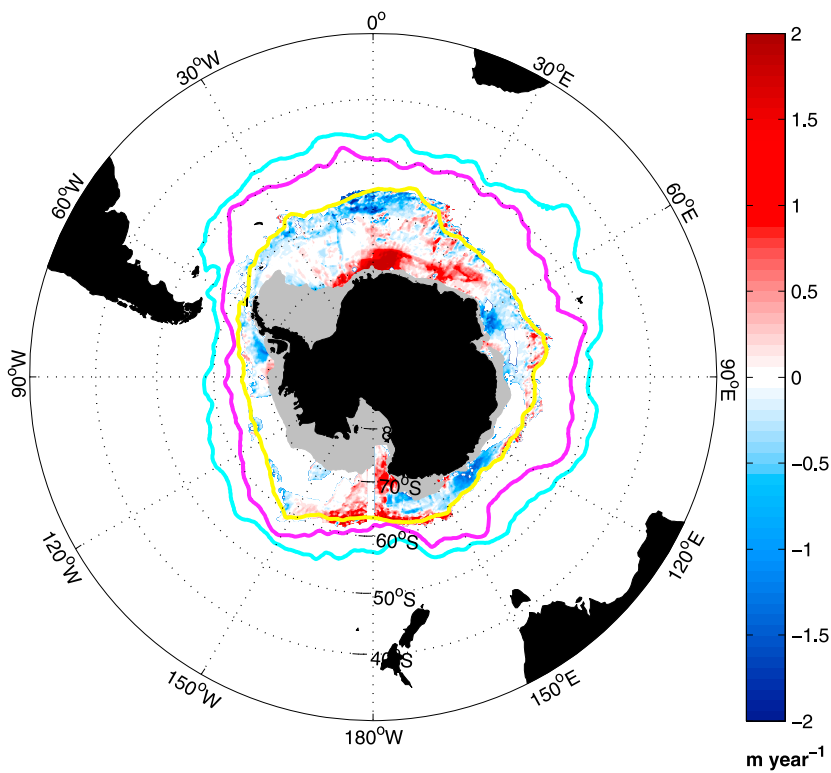


**Figure 11.** Annual mean sea ice advection. The annual mean is calculated as the mean over 2006–2010. The Polar Front (cyan) and Subantarctic Front (magenta) are included [Sallée *et al.*, 2008]. The winter sea ice edge (yellow) is the mean location of the 15% sea ice concentration in August during 2006–2010. The gray shaded area is within the summer sea ice edge, estimated as the mean 15% sea ice concentration in February during 2006–2010.

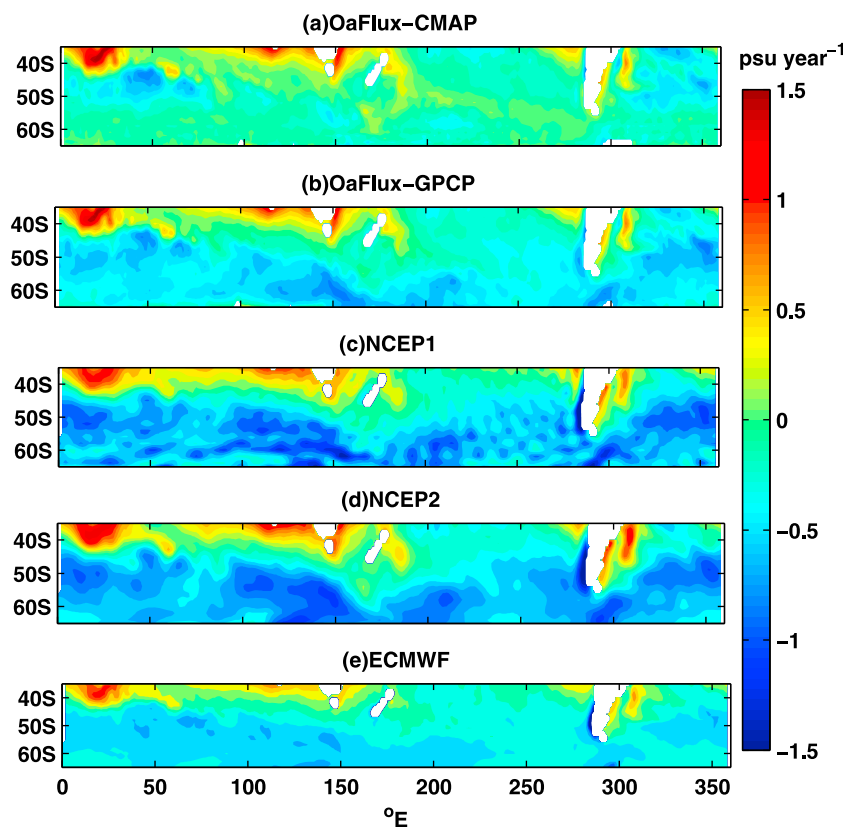


**Figure 12.** The annual mean of the freshwater flux term (first term in equation (1) for different E-P sets: (a) OaFlux-CMAP, (b) OaFlux-GPCP, (c) NCEP1, (d) NCEP2, and (e) ECMWF. The unit is  $\text{psu yr}^{-1}$ . The availability of NCEP1 and NCEP2 are from January 2006 to December 2010, ECMWF is from January 2006 to October 2010, OaFlux is from January 2006 to July 2010, and GPCP and CMAP are from January 2006 to September 2009.

from the Weddell Sea. Some indication of surface freshening in summer is present in the near-surface salinity observations (Figure 2) suggestive of a seasonal meltwater pulse. Localized, intense convergence occurs off the West Antarctic Peninsula, Adelie Land ( $120^{\circ}\text{E}$ – $150^{\circ}\text{E}$ ) and west of Prydz Bay near  $70^{\circ}\text{E}$ .

### 3.7. Temporal Coverage and Annual Mean

[31] The OaFlux evaporation and CMAP precipitation are available from January 2006 to July 2010 and January 2006 to September 2009, respectively. Thus, the net freshwater flux term is calculated from January 2006 to September 2009. The geostrophic advection is calculated from January 2006 to March 2010. The entrainment is estimated from January 2006 to September 2009. Both the salinity tendency and diffusion term are calculated from January 2006 to December 2010. Finally, the sea ice term is estimated from January 2006 to August 2010.

[32] The annual means of the five different sets of  $(E - P) S_m/h_m$  are shown in Figure 12. They show that, south of  $45^{\circ}\text{S}$ , precipitation generally dominates evaporation, which indicates that this region is characterized by water vapor convergence. North of  $45^{\circ}\text{S}$ , evaporation dominates precipitation. The distribution of the means is mostly zonal, with the exception of the water vapor convergence (Figure 12, blue area), which intrudes north of  $45^{\circ}\text{S}$  in both the southeast

Pacific Ocean and the Atlantic Ocean. The Oaflux-GPCP set shows greater magnitudes south of  $45^{\circ}\text{S}$  than does the Oaflux-CMAP set, indicating that the precipitation in GPCP shows greater values than CMAP in this area. The NCEP1 (Figure 12c) and NCEP2 (Figure 12d) both show stronger precipitation in the Atlantic Ocean and between  $0^{\circ}$  and  $150^{\circ}\text{E}$  along ACC compared with ECMWF. The Oaflux-CMAP set was found to be the best in the mixed layer salinity budget according to simple error standards (Appendix A) and will be used in the description of the mixed layer salt budget.

[33] The mean state of the vertical salinity profile implies that entrainment generally increases the mixed layer salinity south of  $45^{\circ}\text{S}$ . It is stronger south of  $55^{\circ}\text{S}$  in the Indian and Atlantic Oceans, and weaker in the western Pacific Ocean (Figure 13b). The annual mean Ekman advection basically reduces the mixed layer salinity in this region (Figure 13c), and has a greater influence near the fronts of the ACC and between  $45^{\circ}\text{S}$  and  $50^{\circ}\text{S}$  in the Atlantic Ocean. This is due to the freshwater brought from the south by the westerly wind. For the annual mean geostrophic advection (Figure 13d), red and blue areas alternate throughout most of the whole basin, indicating small-scale spatial features. Horizontal eddy diffusivity is set to be  $4000 \text{ m}^2 \text{ s}^{-1}$  in this calculation, based on averaged diffusivity estimates from a recent study by Sallée *et al.* [2008]. Diffusivity is a spatially variable quantity and this value may be an overestimate within and south of the

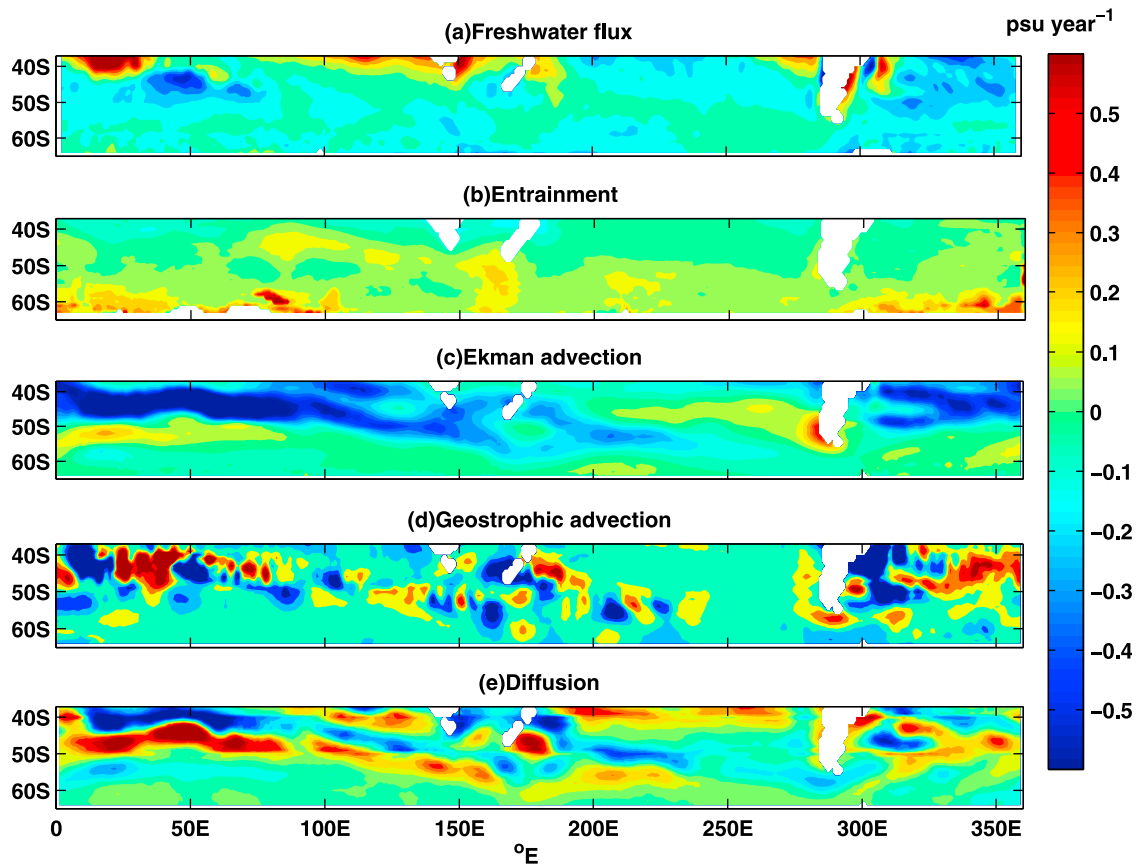


**Figure 13.** The annual mean of each term on the right side of equation (1) but sea ice term: (a) freshwater flux (OAFflux-CMAP), (b) entrainment, (c) Ekman advection, (d) geostrophic advection, and (e) diffusion. The unit is  $\text{psu yr}^{-1}$ .

ACC but serves to quantify a plausible role for mesoscale mixing at the surface. Note, however, that diffusion coefficient estimates are themselves the subject of ongoing research. The resulting horizontal diffusion term (Figure 13e) shows higher magnitudes between 30°E and 70°E in the Indian Ocean, western Pacific, western Atlantic, and along the ACC.

### 3.8. Domain Average

[34] Domain (45°S–62°S) averages of each term except the sea ice term on the right-hand side of equation (1) (Figure 14a) show that entrainment, net freshwater flux and Ekman advection have strong seasonal variations and make important contributions to the seasonal variation of the mixed layer salinity. The diffusion and geostrophic advection are at least an order of magnitude smaller than the other terms when averaged this way. The smaller magnitude in the net geostrophic advection is due to the summation of stronger positive and negative values canceling each other. Thus, while the overall effect of the geostrophic advection is small, its contribution to the mixed layer salinity seasonal variation, like that of horizontal diffusion, is important locally. The mixed layer salinity budget is analyzed in smaller regions in Appendix B in order to show the local contribution of the horizontal diffusion and geostrophic advection terms.

[35] The seasonal variation of the salinity tendency can be partly captured by the sum of the forcing terms without sea ice

on the right-hand side of equation (1) (Figure 14b). However, its difference (Figure 14c) shows the greatest difference in spring (OND) with the salinity tendency lower than the forcing. The differences in each spring (OND) (Figure 14c) are beyond expected 0.12  $\text{psu yr}^{-1}$  uncertainties estimated in Appendix C (except in 2007). Thus, a seasonal characterization of the difference is again suggestive of a sea ice effect, as sea ice starts to melt in spring. The large uncertainties in the salinity budget come mainly from the net freshwater flux (Appendix C) implying that a better freshwater flux is necessary to improve the agreement of the salinity budget.

[36] In order to emphasize the role of the sea ice, the domain average is also done for the area 50°S–62°S and 55°S–62°S. The role of sea ice becomes larger toward the south (Figure 15), particularly in spring. In order to quantify this, Table 1 shows RMS increases from 0.080 to 0.141 in the three domains and the greatest difference appearing in spring in the domain 55°S–62°S (Figure 15c).

[37] The mixed layer salinity budget is improved by different amounts in the three domains by including sea ice (Table 1). For the domain 45°S–62°S, the mixed layer salinity budget has been improved, with a 25% decrease in RMS imbalance. Likewise, the mixed layer salinity budget has been improved by 28% and 36% in the domains 50°S–62°S and 55°S–62°S, respectively. The total forcing shows much better agreement with the salinity tendency in all three

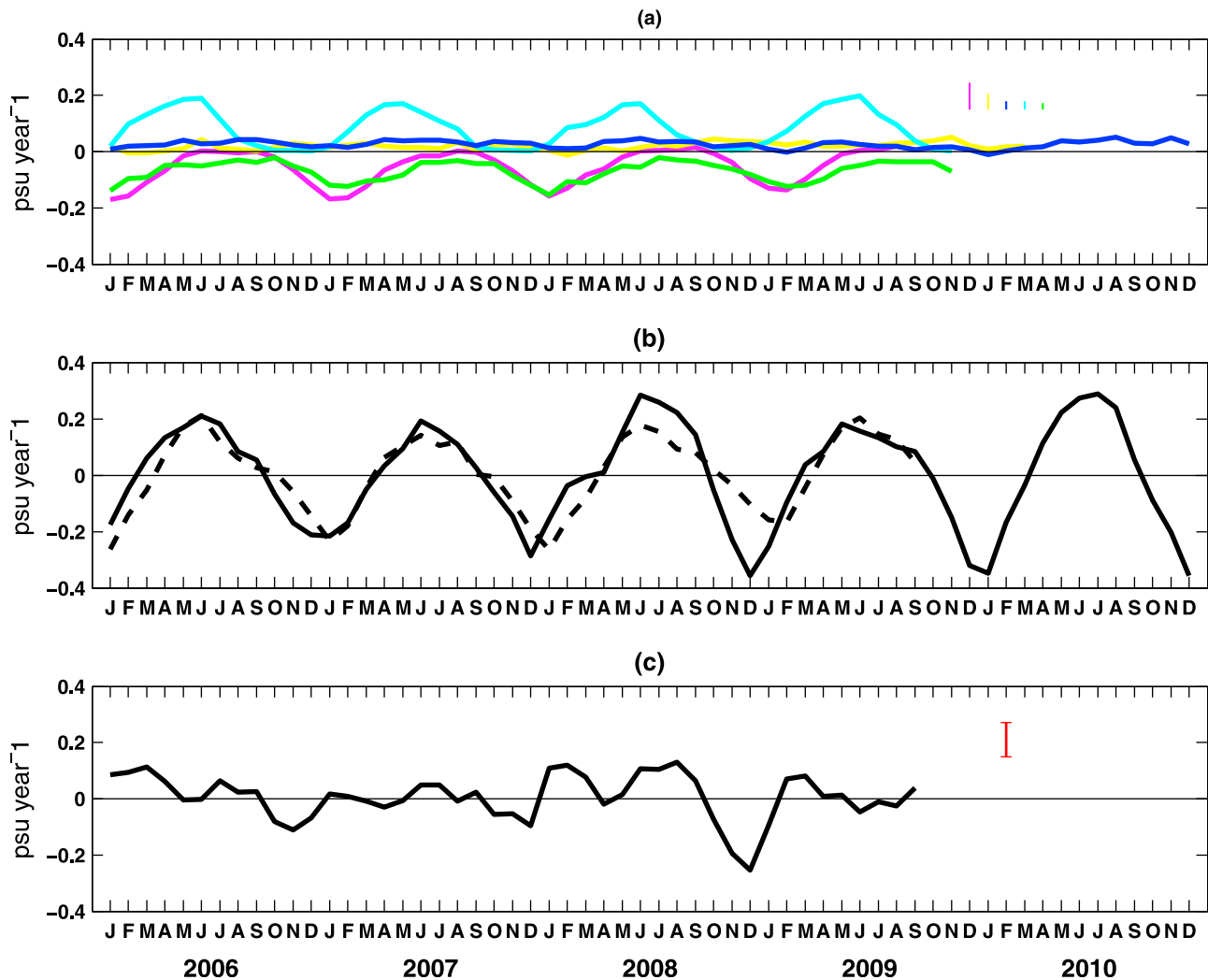


**Figure 14.** Domain- ( $45^{\circ}\text{S}$ – $62^{\circ}\text{S}$ ) averaged character for the terms in equation (1) during 2006–2010. (a) Forcing terms: the cyan line is for the entrainment, the magenta line is for net freshwater flux, the green line is for the Ekman advection, the yellow line is for the geostrophic advection, and the blue line is for the diffusion, the vertical lines are the associated errors for the forcing term (Appendix C) of the same color. (b) The sum of the forcing terms in Figure 14a (dashed black line) and the domain-averaged salinity tendency (solid black line) and (c) the difference of the domain average salinity tendency and the sum of the forcings in Figure 14b, which is estimated by subtracting the sum of the forcings from the salinity tendency. The red bar in Figure 14c shows the estimated total errors (Appendix C) in the salinity budget.

domains (Figure 15), and in particular, sea ice effects reduce the deficiency in spring.

#### 4. Summary and Discussion

[38] Between  $45^{\circ}\text{S}$  and  $62^{\circ}\text{S}$  in the Southern Ocean, the near-surface salinity has a seasonal variation, saltier in winter and fresher in summer. The net freshwater flux and Ekman advection tend systematically to reduce the mixed layer salinity, while the entrainment, geostrophic advection and diffusion tend to increase the mixed layer salinity. The entrainment, net freshwater flux and Ekman advection all have seasonal variations and play similar roles in the seasonal variation of the mixed layer salinity variation. The geostrophic advection and diffusion are smaller in the domain average,

but their roles are likely important locally as described in Appendix B.

[39] The main new result of our estimates compared to Dong *et al.* [2009] is the quantification of the sea ice contribution to the upper ocean salinity balance. Another major addition is that the period of this study is longer, from 2006 to 2010, hence including substantially more data, and also that unlike Dong *et al.* [2009] the time period is consistent for all the data sets, likely reducing bias. Additionally, more freshwater flux products are used in this study, producing a more complete analysis of the upper ocean mixed layer salinity budget and errors. The treatment of mixed layer entrainment is consistent with other studies [Wang and McPhaden, 2000, 1999; Hayes *et al.*, 1991]. Here,  $\Delta S$  is defined as the salinity difference between the average salinity within the mixed

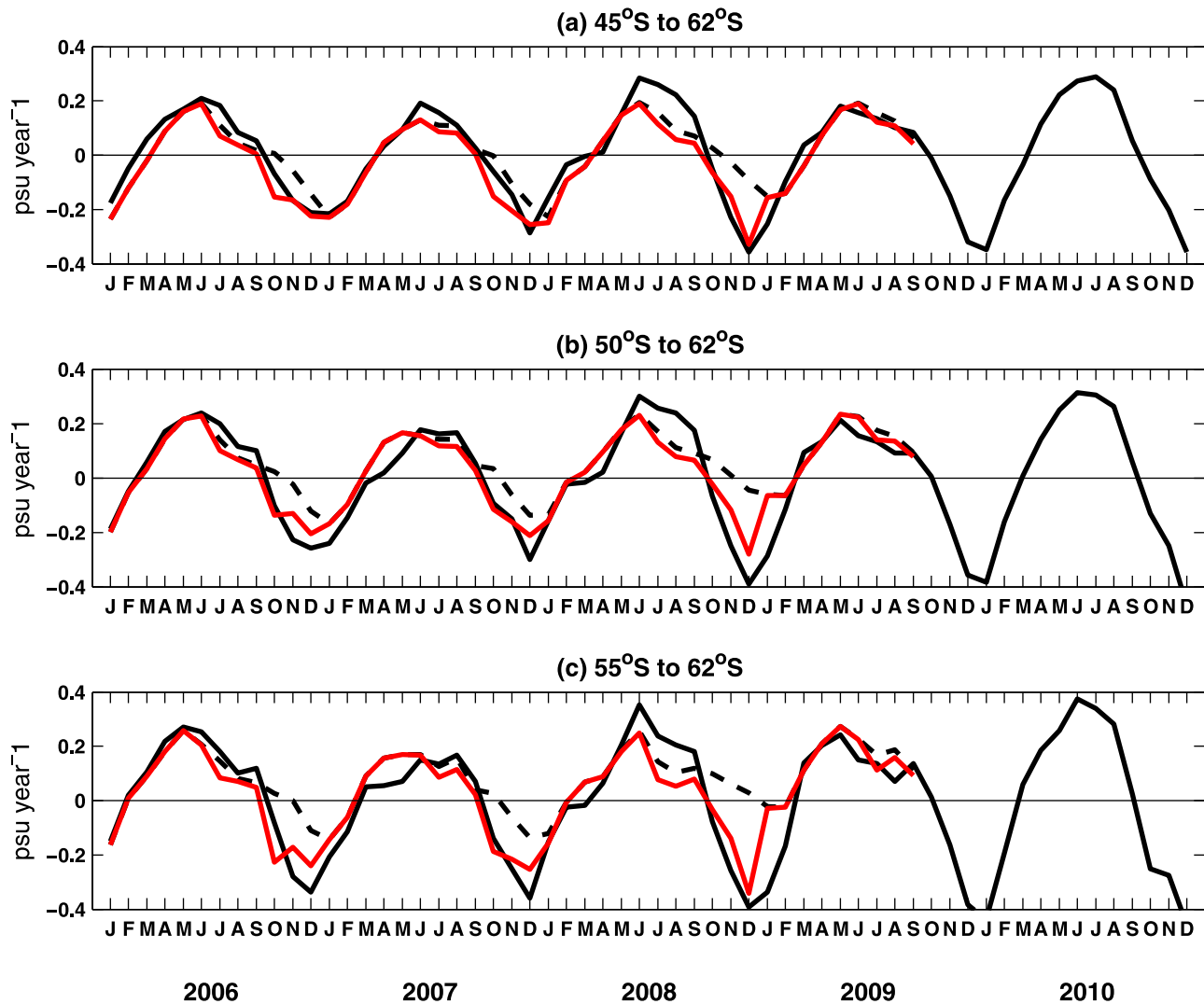


**Figure 15.** Domain-averaged salinity tendency, sum of forcing terms without sea ice and with sea ice. The solid black line shows the salinity tendency, the dashed black line shows the sum of forcing without sea ice, and the red line shows the sum of forcing with sea ice: (a) 45°S–62°S, (b) 50°S–62°S, and (c) 55°S–62°S.

layer and 15 m below the base of the mixed layer instead of immediately below the mixed layer as with *Dong et al.* [2009]. However, different methodologies tested in the entrainment velocity calculation result in similar amounts of the entrainment.

[40] We quantify the sea ice contribution in the mixed layer salinity budget and conclude that it has a significant effect, and the importance of the sea ice increases toward the continent. Thus, although the sea ice contribution is small in the larger, more northerly domains examined by *Dong et al.* [2009], it is significant overall, and cannot be neglected in salinity budgets of the Southern Ocean south of the Polar Front. Sea ice fluxes more generally need to be taken into account in climate simulations to predict salinity variability in the upper ocean.

[41] As the seasonal salinity observations from Argo are essentially limited to latitudes up to about 62°S at present and the sea ice term is generally stronger near the southern boundary of our domain, a detailed investigation of the large-scale spatial character of the sea ice contribution close to the

continent is difficult to pursue until more observations become available in the sea ice zone. However, our study, for the first time, quantifies the role of sea ice in the mixed layer salinity budget outside the seasonal sea ice zone in the Southern Ocean.

[42] Unfortunately, the mixed layer salinity budget is still not entirely closed (Figure 15 and Table 1). This could be due to several factors, including the limitation of the observations, the air sea freshwater flux errors, and the estimates of

**Table 1.** The RMS of the Difference Between the Left-Hand Side of Equation (1) and the Sum of Right-Hand Side of Equation (1) With Sea Ice and Without Sea Ice in the Latitude Bands 45°S–62°S, 50°S–62°S, and 55°S–62°S<sup>a</sup>

RMS	45°S–62°S	50°S–62°S	55°S–62°S
no sea ice	0.080	0.103	0.141
with sea ice	0.060	0.076	0.091

<sup>a</sup>The unit is  $\text{psu yr}^{-1}$ .

**Table A1.** The RMS of the Difference Between the Domain-Averaged ( $45^{\circ}\text{S}$ – $62^{\circ}\text{S}$ ) Sum of the Right-Hand Side of Equation (1) Without Sea Ice Term and the Left-Hand Side of Equation (1) for Different Freshwater Fluxes and  $\Delta S^a$

	ECMWF	NCEP1	NCEP2	OAFflux-CMAP	OAFflux-GPCP
$\Delta S_0$	0.179	0.246	0.249	0.125	0.199
$\Delta S_5$	0.147	0.216	0.218	0.101	0.168
$\Delta S_{10}$	0.128	0.195	0.198	0.088	0.148
$\Delta S_{15}$	0.115	0.181	0.184	0.080	0.134
$\Delta S_{20}$	0.217	0.256	0.258	0.198	0.226

<sup>a</sup>For each combination of the freshwater flux and  $\Delta S$ , all the other terms in equation (1) remain the same. The unit is  $\text{psu yr}^{-1}$ .

entrainment. Based on the error analysis in Appendix C, the dominant uncertainties in the salinity budget are mostly from the precipitation. Thus, a better freshwater flux is needed to improve further the mixed layer salinity budget. In addition, the sea ice mass estimation itself is fairly rough. As more salinity measurements under sea ice become available from the Argo profiling floats and animal borne CTD (conductivity–temperature–depth) sensors, a better determination of the salinity budget with sea ice could be accomplished. Ultimately, an inversion of seasonal salinity data with constraints on air–sea fluxes and ice thickness might be possible.

### Appendix A: Sensitivity of the Mixed Layer Salinity Budget to Various Data

[43] The results shown in section 3 are the best estimates according to the RMS of the imbalance in the mixed layer salinity budget from the existing data.

[44] The freshwater flux data used in this sensitivity test includes the ECMWF, NCEP1, NCEP2, OAFflux, GPCP, and CMAP. As discussed in section 3.2, these freshwater fluxes produce five sets of E–P and have been applied to the mixed layer salinity budget. The appropriate salinity difference ( $\Delta S$ ) at the base of the mixed layer is difficult to specify and we examined it in five ways: difference between average salinity within the mixed layer and at the base of the mixed layer; difference between average salinity within the mixed layer and 5 m below the base of the mixed layer; difference between average salinity within the mixed layer and 10 m below the mixed layer; difference between average salinity within the mixed layer and 15 m below the mixed layer; and difference between average salinity within the mixed layer and 20 m below the mixed layer. The results (Table A1) show that beyond 15 m, the choice of submixed layer salinity does not provide a reasonable estimate of the entrainment.

[45] To make use of the various data discussed above, 25 experiments are done to find the best estimates of the mixed layer salinity budget with various choices of the data being discussed above and the same Ekman advection, geostrophic advection, diffusion and salinity tendency. For this process, the sea ice term is not included. The RMS of each experiment is shown in Table A1. Based on the 25 experiments, the combination of the freshwater flux of OAFflux–CMAP and  $\Delta S$ , defined as the difference between average salinity within the mixed layer and 15 m below the mixed layer, estimates the best mixed layer salinity budget with a minimum RMS of  $0.080 \text{ psu yr}^{-1}$  (Table A1). This procedure could be carried out formally with inverse techniques but given the limited

scope of this study it was not thought appropriate to develop that approach. Our basic results should not be too sensitive to the details of the method but this question needs to be further explored in the context of large-scale ocean state estimates.

### Appendix B: The Local Importance of the Geostrophic Advection and Horizontal Diffusion

[46] The area of  $45^{\circ}\text{S}$ – $55^{\circ}\text{S}$  and  $10^{\circ}\text{E}$ – $80^{\circ}\text{E}$ , where diffusion peaks and shows consistent positive sign (Figure 13e), is selected to show the local contribution of the horizontal diffusion in the salinity budget. The seasonal variation of the mixed layer salinity in this region (Figure B1b) is similar to the larger domain (Figure 14b), while the contribution of each term is quite different. Here, the net freshwater flux and Ekman advection reduce the salinity and both peak in summer; the geostrophic advection generally increases the salinity but its contribution is small compared with other terms; the entrainment increases the salinity and shows a maximum in late fall and early winter; the diffusion term does not show very much seasonal variation but makes the largest contribution to the salinity change during the year (Figure B1a). Thus, unlike the domain average salinity budget (Figure 14a), in smaller regions the horizontal diffusion plays an important role.

[47] The area of  $40^{\circ}\text{S}$ – $53^{\circ}\text{S}$  and  $30^{\circ}\text{W}$ – $5^{\circ}\text{E}$ , where geostrophic advection shows a consistent positive sign, (Figure 13d), is selected to show the local contribution of the geostrophic advection in the salinity budget. The seasonal variation of the mixed layer salinity in this region (Figure B2b) is again similar to the larger domain (Figure 14b). Here, the net freshwater flux and Ekman advection reduce the salinity and both peak in summer; Ekman advection dominates the net freshwater flux. The entrainment increases the salinity and peaks in late fall and early winter; the diffusion term does not show very much seasonal variation; the geostrophic advection increases the mixed layer salinity locally and it makes the largest contribution among the three terms that increase the mixed layer salinity (Figure B2a). Thus, unlike the salinity budget in Figure 14a, in this region the geostrophic advection term plays an important role in the salinity budget.

[48] These two examples suggest that the contribution of the various forcing terms in equation (1) to the mixed layer salinity is dependent on the region, and the area. In this paper, we concentrate on the higher latitude balances where localized areas of intense salinity diffusion and geostrophic current exist but are less important.

### Appendix C: Error Estimate

[49] The errors associated with the upper ocean salinity budget including the freshwater flux (precipitation and evaporation), the geostrophic advection, the Ekman advection, the entrainment, the diffusion, and the salinity tendency are estimated here as domain- and temporal averaged values (Figure 14a). The method adopted here is based on *Ren and Riser* [2009].

[50] For each of the forcing terms (right-hand side of equation (1)) the standard errors are estimated. As the precipitation, evaporation, and entrainment have larger uncertainties than the geostrophic advection and Ekman advection,

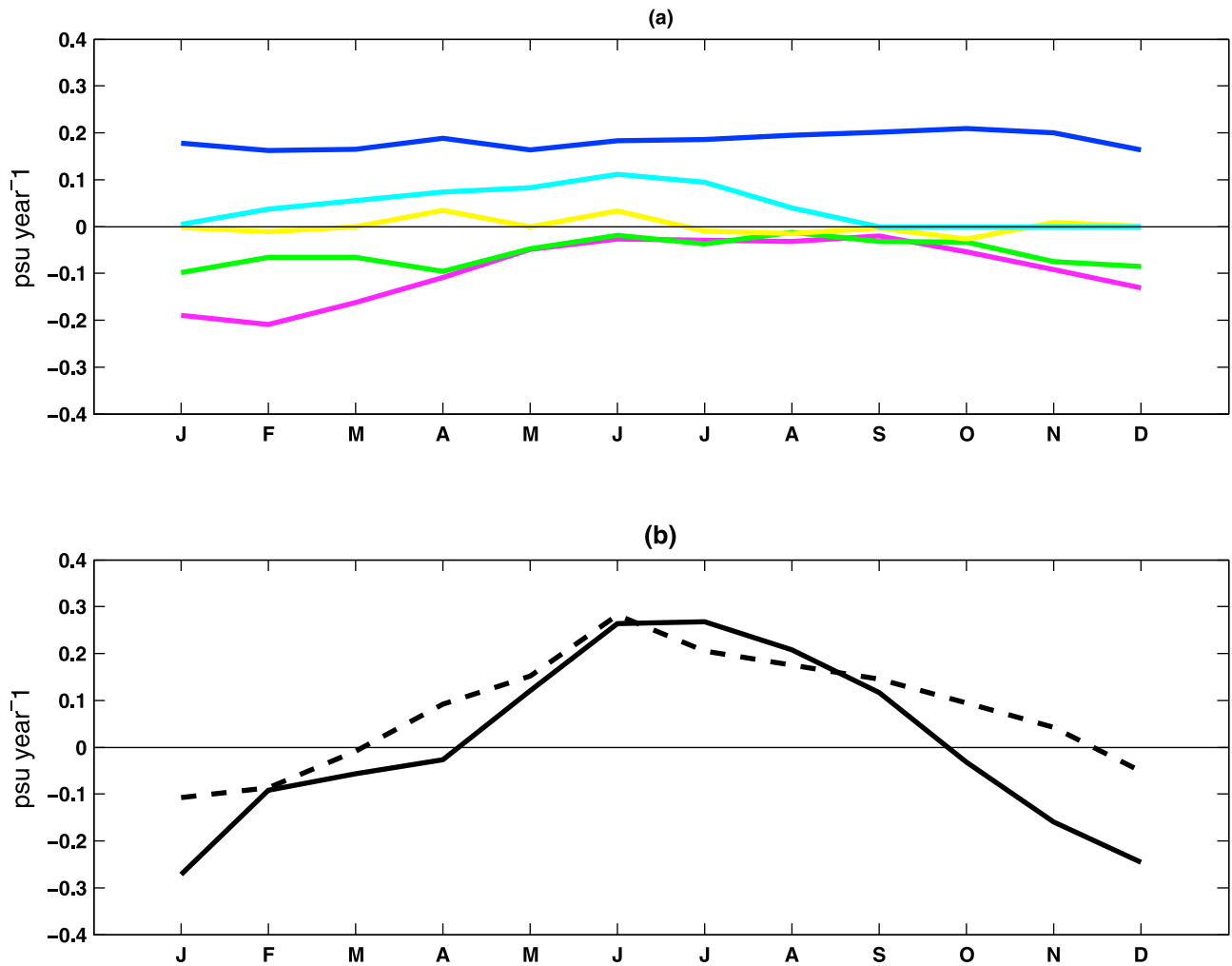


**Figure B1.** Domain- ( $45^{\circ}\text{S}$ – $55^{\circ}\text{S}$  and  $10^{\circ}\text{E}$ – $80^{\circ}\text{E}$ ) averaged seasonal character for the terms in equation (1), being estimated from the average of each month during 2006–2010. The lines show the (a) forcing terms: the cyan line is for the entrainment, the magenta line is for freshwater flux, the green line is for the Ekman advection, the yellow line is for the geostrophic advection, and the blue line is for the diffusion. (b) The sum of the forcing terms in Figure 16a (dashed black line) and the domain-averaged salinity tendency (solid black line).

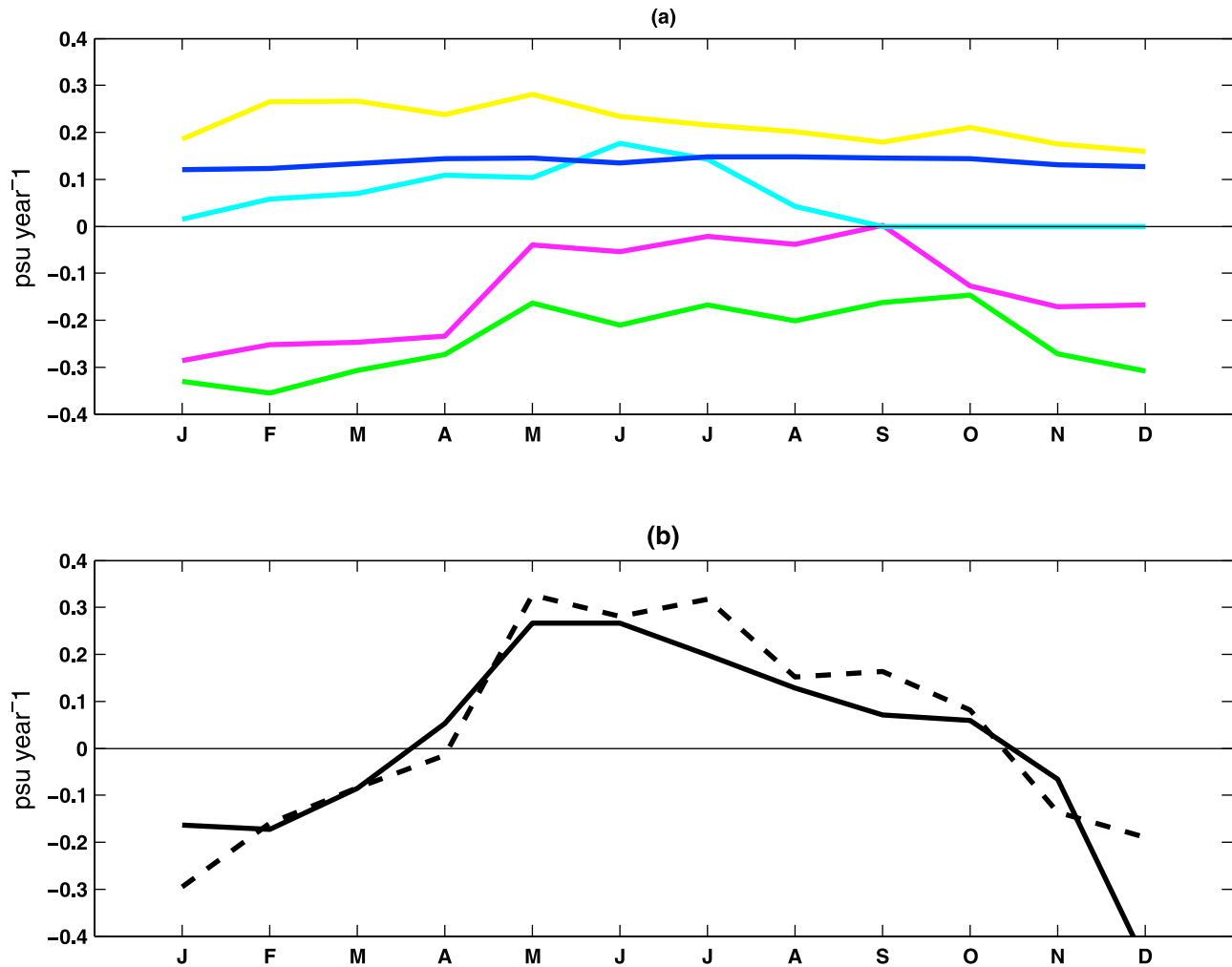


**Figure B2.** Domain- ( $40^{\circ}\text{S}$ – $53^{\circ}\text{S}$  and  $30^{\circ}\text{W}$ – $5^{\circ}\text{E}$ ) averaged seasonal character for the terms in equation (1), being estimated from the average of each month during 2006–2010. The lines show the (a) Forcing terms: the cyan line is for the entrainment, the magenta line is for freshwater flux, the green line is for the Ekman advection, the yellow line is for the geostrophic advection, and the blue line is for the diffusion. (b) The sum of the forcing terms in Figure 17a (dashed black line) and the domain-averaged salinity tendency (solid black line).

uncertainties associated with these terms are calculated separately. For the precipitation, the errors including the algorithm and sampling errors provided by CMAP are estimated. The  $8 \text{ Wm}^{-2}$  uncertainties [Jin et al., 2006] in the latent heat flux are considered in the evaporation. A 10 m uncertainty in the mixed layer depth estimation [Ren and Riser, 2009] is included in the entrainment estimate. The errors associated with the salinity tendency (left-hand side of equation (1)) are mainly from the sampling errors and are estimated following Ren and Riser [2009]. The result is  $0.02 \text{ psu yr}^{-1}$ , with a decreasing trend from 2006 to 2010 due to the improvement of the sampling.

[51] Based on the summation rule of the error propagation [Ren and Riser, 2009], the total error in the mixed layer salinity budget in a domain and temporal average is  $0.12 \text{ psu yr}^{-1}$  (Figure 14c), with the errors from precipitation and evaporation term  $0.10 \text{ psu yr}^{-1}$ ; the geostrophic advection term  $0.06 \text{ psu yr}^{-1}$ ; the Ekman advection term  $0.04 \text{ psu yr}^{-1}$ ; the diffusion term  $0.03 \text{ psu yr}^{-1}$  and the entrainment term  $0.03 \text{ psu yr}^{-1}$ . The  $0.10 \text{ psu yr}^{-1}$  uncertainty from evaporation and precipitation accounts for more than 80% of the total errors, among which the precipitation makes the largest contribution.

[52] **Acknowledgments.** Support from NSF OCE-0622670 and NSF OCE-0822075 is acknowledged. We also thank the two anonymous reviewers for their helpful comments, which contributed significantly to the improvement of the work. T. Worby provided help with sea ice thickness data.

## References

- Adler, R. F., et al. (2003), The version 2 Global Precipitation Climatology Project (GPCP) monthly precipitation analysis (1979–present), *J. Hydrometeorol.*, *4*, 1147–1167, doi:10.1175/1525-7541(2003)004<1147:TVGPCP>2.0.CO;2.
- Banks, H. T., and N. L. Bindoff (2003), Comparison of observed temperature and salinity changes in the Indo-Pacific with results from the coupled climate model HadCM3: Processes and mechanisms, *J. Clim.*, *16*, 156–166, doi:10.1175/1520-0442(2003)016<0156:COOTAS>2.0.CO;2.
- Berrisford, P., D. Dee, K. Fielding, M. Fuentes, P. Kallberg, S. Kobayashi, and S. Uppala (2009), The ERA-Interim archive, report, Eur. Cent. for Medium-Range Weather Forecasts, Reading, U. K.
- Böning, C. W., A. Disper, M. Visbeck, S. R. Rintoul, and F. U. Schwarzkopf (2008), The response of the Antarctic Circumpolar Current to recent climate change, *Nat. Geosci.*, *1*, 864–869, doi:10.1038/ngeo362.
- Bretherton, F. P., R. E. Davis, and C. B. Fandry (1976), A technique for objective analysis design of oceanographic experiments allied to mode 73, *Deep Sea Res.*, *23*, 559–582.
- Centre National d'Etudes Spatiales (1996), *Aviso User Handbook: Merged TOPEX/POSEIDON Products*, 3rd ed., Toulouse, France.
- Charrassin, J. B., et al. (2008), Southern Ocean frontal structure and sea ice formation rates revealed by elephant seals, *Proc. Natl. Acad. Sci. U. S. A.*, *105*, 11,634–11,639.
- Comiso, J. C., and F. Nishio (2008), Trends in the sea ice cover using enhanced and compatible AMSR-E, SSM/I, and SMMR data, *J. Geophys. Res.*, *113*, C02S07, doi:10.1029/2007JC004257.
- de Boyer Montégut, C., G. Madec, A. S. Fisher, A. Lazar, and D. Iudicone (2004), Mixed layer depth over the global ocean: An examination of profile data and a profile-based climatology, *J. Geophys. Res.*, *109*, C12003, doi:10.1029/2004JC002378.
- Dong, S., J. Sprintall, S. T. Gille, and L. Talley (2008), Southern Ocean mixed-layer depth from Argo float profiles, *J. Geophys. Res.*, *113*, C06013, doi:10.1029/2006JC004051.
- Dong, S., S. L. Garzoli, and M. Baringer (2009), An assessment of the seasonal mixed layer salinity budget in the Southern Ocean, *J. Geophys. Res.*, *114*, C12001, doi:10.1029/2008JC005258.
- Durack, P. J., and S. E. Wijffels (2010), Fifty-year trends in global ocean salinities and their relationship to broad-scale warming, *J. Clim.*, *23*, 4342–4362, doi:10.1175/2010JCLI3377.1.
- Gould, J., et al. (2004), Argo profiling floats bring new era of in situ ocean observation, *Eos Trans. AGU*, *85*(19), 179,190–191, doi:10.1029/2004EO190002.
- Hayes, S. P., P. Chang, and M. J. McPhaden (1991), Variability of the sea-surface temperature in the eastern equatorial Pacific during 1986–1988, *J. Geophys. Res.*, *96*, 10,553–10,566, doi:10.1029/91JC00942.
- Huffman, G. J., R. F. Adler, P. Arkin, A. Chang, R. Ferraro, A. Gruber, J. Janowiak, A. McNab, B. Rudolf, and U. Schneider (1997), The global precipitation climatology project (GPCP) combined precipitation dataset, *Bull. Am. Meteorol. Soc.*, *78*, 5–20, doi:10.1175/1520-0477(1997)078<0005:TGPCPG>2.0.CO;2.
- Jacobs, S. J., and C. F. Giulivi (2010), Large multi-decadal salinity trends near the Pacific–Antarctic continental margin, *J. Clim.*, *23*, 4508–4524, doi:10.1175/2010JCLI3284.1.
- Jin, X., L. Yu, and R. Weller (2006), Evaluation of global heat flux from the WHOI OAF flux, ISCPP, and atmospheric reanalysis, *Eos Trans. AGU*, *87*(52), Fall Meet. Suppl., Abstract OS41A-0567.
- Kalnay, E., et al. (1996), The NCEP/NCAR 40-year reanalysis project, *Bull. Am. Meteorol. Soc.*, *77*, 437–471, doi:10.1175/1520-0477(1996)077<0437:TNYRP>2.0.CO;2.
- Kanamitsu, M., W. Ebisuzaki, J. Woollen, S. K. Yang, J. J. Hnilo, M. Fiorino, and G. L. Potter (2002), NCEP–DOE AMIP-II reanalysis (R-2), *Bull. Am. Meteorol. Soc.*, *83*, 1631–1643, doi:10.1175/BAMS-83-11-1631.
- Le Traon, P. Y. (1990), A method for optimal analysis of fields with spatially variable mean, *J. Geophys. Res.*, *95*, 13,543–13,547, doi:10.1029/JC095iC08p13543.
- Martinson, D. G., and C. Wamser (1990), Ice drift and momentum exchange in winter Antarctic pack ice, *J. Geophys. Res.*, *95*, 1741–1755, doi:10.1029/JC095iC02p01741.
- Pegion, P. J., M. A. Bourassa, D. M. Legler, and J. J. O'Brien (2000), Objectively derived daily “winds” from satellite scatterometer data, *Mon. Weather Rev.*, *128*, 3150–3168, doi:10.1175/1520-0493(2000)128<3150:ODDWFS>2.0.CO;2.
- Ren, L., and S. C. Riser (2009), Seasonal salt budget in the northeast Pacific Ocean, *J. Geophys. Res.*, *114*, C12004, doi:10.1029/2009JC005307.
- Rintoul, S. R., and M. H. England (2002), Ekman transport dominates local air-sea fluxes in driving variability of Subantarctic Mode water, *J. Phys. Oceanogr.*, *32*, 1308–1321, doi:10.1175/1520-0485(2002)032<1308:ETDLAS>2.0.CO;2.
- Rio, M.-H., P. Schaeffer, and J. M. Lemoine (2005), Estimation of the ocean mean dynamic topography through the combination of altimetric data, in-situ measurements and GRACE geoid: From global to regional studies, paper presented at GOCINA International Workshop, Cent. Eur. de Géodyn. et de Séismol., Luxembourg, 13–15 Apr.
- Rio, M.-H., P. Schaeffer, G. Moreaux, J.-M. Lemoine, and E. Bronner (2009), A new mean dynamic topography computed over the global ocean from GRACE data, altimetry and in-situ measurements, paper presented at OceanObs09 Symposium, Eur. Space Agency, Venice, Italy, 21–25 Sept.
- Sallée, J.-B., N. Wienders, K. Speer, and R. Morrow (2006), Formation of subantarctic mode water in the southeastern Indian Ocean, *Ocean Dyn.*, *56*, 525–542, doi:10.1007/s10236-005-0054-x.
- Sallée, J. B., K. Speer, R. Morrow, and R. Lumpkin (2008), An estimate of Lagrangian eddy statistics and diffusion in the mixed layer of the Southern Ocean, *J. Mar. Res.*, *66*, 441–463, doi:10.1357/002224008787157458.
- Spreen, G., L. Kaleschke, and G. Heygster (2008), Sea ice remote sensing using AMSR-E 89-GHz channels, *J. Geophys. Res.*, *113*, C02S03, doi:10.1029/2005JC003384.
- Stammerjohn, S. E., D. G. Martinson, R. C. Smith, X. Yuan, and D. Rind (2008), Trends in Antarctic annual sea ice retreat and advance and their relation to El Niño–Southern Oscillation and Southern Annular Mode variability, *J. Geophys. Res.*, *113*, C03S90, doi:10.1029/2007JC004269.
- Tumer, J., R. Bindshadler, P. Convey, G. di Prisco, E. Fahrback, J. Gutt, D. Hodgson, P. Mayewski, and C. Summerhayes (2009), *Antarctic Climate Change and the Environment*, 526 pp., Sci. Comm. on Antarctic Res., Cambridge, U. K.
- Wang, W., and M. J. McPhaden (1999), The surface-layer heat balance in the equatorial Pacific Ocean. Part 1: Mean seasonal cycle, *J. Phys. Oceanogr.*, *29*, 1812–1831, doi:10.1175/1520-0485(1999)029<1812:TSLHBI>2.0.CO;2.
- Wang, W., and M. J. McPhaden (2000), The surface-layer heat balance in the equatorial Pacific Ocean. Part 2: Interannual variability, *J. Phys. Oceanogr.*, *30*, 2989–3008, doi:10.1175/1520-0485(2001)031<2989:TSLHBI>2.0.CO;2.
- Wong, A. P. S., N. L. Bindoff, and J. A. Church (1999), Large-scale freshening of intermediate waters in the Pacific and Indian Oceans, *Nature*, *400*, 440–443, doi:10.1038/22733.

- Worby, A. P., C. A. Geiger, M. J. Paget, M. L. Van Woert, S. F. Ackley, and T. L. DeLiberty (2008), Thickness distribution of Antarctic sea ice, *J. Geophys. Res.*, *113*, C05S92, doi:10.1029/2007JC004254.
- Xie, P., and P. A. Arkin (1996), Analyses of global monthly precipitation using gauge observations, satellite estimates, and numerical model predictions, *J. Clim.*, *9*, 840–858, doi:10.1175/1520-0442(1996)009<0840:AOGMPU>2.0.CO;2.
- Xie, P., and P. A. Arkin (1997), Global precipitation: A 17-year monthly analysis based on gauge observations, satellite estimates, and numerical model outputs, *Bull. Am. Meteorol. Soc.*, *78*, 2539–2558, doi:10.1175/1520-0477(1997)078<2539:GPAYMA>2.0.CO;2.
- Yelland, M., and P. K. Taylor (1996), Wind stress measurements from the open ocean, *J. Phys. Oceanogr.*, *26*, 541–558, doi:10.1175/1520-0485(1996)026<0541:WSMFTO>2.0.CO;2.
- Yu, L., and R. A. Weller (2007), Objectively analyzed air-sea heat fluxes for the global ice-free oceans (1981–2005), *Bull. Am. Meteorol. Soc.*, *88*, 527–539, doi:10.1175/BAMS-88-4-527.
- 
- E. P. Chassignet, Center for Ocean-Atmospheric Prediction Studies, Florida State University, 200 R. M. Johnson Bldg., Tallahassee, FL 32306-2840, USA.
- L. Ren (corresponding author), Earth System Science Interdisciplinary Center, Cooperative Institute for Climate and Satellites, University of Maryland, College Park, MD 20740, USA. (lren@umd.edu)
- K. Speer, Department of Earth, Ocean and Atmospheric Science, Florida State University, 1017 Academic Way, PO Box 3064520, Tallahassee, FL 32306-4520, USA.